

# Tempo-Spatial Compressed Sensing of Organ-on-a-Chip for Pervasive Health

Chen Song, *Student Member, IEEE*, Aosen Wang, *Student Member, IEEE*, Feng Lin<sup>1</sup>, *Member, IEEE*, Mohammadnabi Asmani, Ruogang Zhao, Zhanpeng Jin<sup>2</sup>, *Senior Member, IEEE*, Jian Xiao, and Wenyao Xu<sup>3</sup>, *Member, IEEE*

**Abstract**—As a micro-engineered biomimetic system to replicate key functions of living organs, organ-on-a-chip (OC) technology provides a high-throughput model for investigating complex cell interactions with both high temporal and spatial resolutions in biological studies. Typically, microscopy and high-speed video cameras are used for data acquisition, which are expensive and bulky. Recently, compressed sensing (CS) has increasingly attracted attentions due to its extremely low-complexity structure and low sampling rate. However, there is no CS solution tailored for tempo-spatial information acquisition. In this paper, we propose tempo-spatial CS (TS-CS), a unified CS architecture for OC stream, which achieves significant cost reduction and truly combines sensing with compression along the temporal and spatial domains. We point out that TS-CS can consistently achieve better performance by exploiting tempo-spatial compressibility in OC data. To this end, we comprehensively evaluate the system performance by employing four different bases for CS. With comparison to the traditional way, we show that TS-CS always obtains better recovery result with a throughput bound and can achieve around 25% throughput improvement under a reconstruction demand by applying discrete cosine transform matrix as the basis.

**Index Terms**—Compressed sensing, organ-on-a-chip, tempo-spatial information acquisition, pervasive health.

Manuscript received May 15, 2017; revised October 5, 2017; accepted November 13, 2017. Date of publication November 20, 2017; date of current version March 5, 2018. This material is based in part on the work supported in part by the National Science Foundation under Grant ECCS-1462498 and in part by the International Science & Technology Cooperation and Exchanges Plan in ShaanXi Province of China under Grant 2016KW-044. An early version [1] was presented at the IEEE Biomedical and Health Informatics Conference 2017. (C. Song, A. Wang, and F. Lin contributed equally to this work.) (Corresponding author: Wenyao Xu.)

C. Song, A. Wang, and W. Xu are with the Department of Computer Science and Engineering, University at Buffalo, the State University of New York, Buffalo, NY 14260 USA (e-mail: csong5@buffalo.edu; aosenwan@buffalo.edu; wenyaoxu@buffalo.edu).

F. Lin is with the Department of Computer Science and Engineering, University of Colorado Denver, Denver, CO 80204 USA (e-mail: feng.2.lin@ucdenver.edu).

M. Asmani and R. Zhao are with the Department of Biomedical Engineering, University at Buffalo, the State University of New York, Buffalo, NY 14260 USA (e-mail: masmani@buffalo.edu; rgzhao@buffalo.edu).

Z. Jin is with the Department of Electrical and Computer Engineering, Binghamton University, the State University of New York, Binghamton, NY 13902 USA (e-mail: zjin@binghamton.edu).

J. Xiao is with the School of Electronics and Control Engineering, Chang'an University, Xi'an 710064 China (e-mail: xiaojian@chd.edu.cn).  
Digital Object Identifier 10.1109/JBHI.2017.2775559

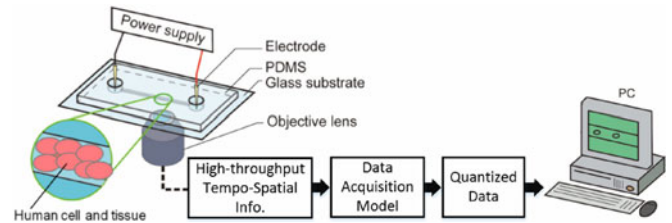


Fig. 1. Overview of the human organs-on-a-chip. Human tissue on the glass substrate is activated by the electrode, then the entire high-throughput tempo-spatial movements of the tissue are recorded by the Data Acquisition Model (DAM) through the lens.

## I. INTRODUCTION

ORGAN-ON-A-CHIP (OC) is a newly emerged technology that seeks to recapitulate the structure and physiological function of native human organs using miniaturized in vitro 3D culture of living cells, and has been envisioned as a promising platform for drug screening and disease modeling in point-of-care (POC) applications [2], [3]. Existing OC devices are mostly made of optical-transparent, biocompatible Polydimethylsiloxane (PDMS) material. In biomedical research, an in vitro model system with the potential to replace resource-limited animal and human experimentation is of high interest. This has been traditionally addressed by centimeter-sized three-dimensional engineered tissues. However, these large constructs typically require millions of cells, have a steep gradient of cell density from the surface to the core, and face diffusional limitations of oxygen and media exchange. Due to its miniature size, OC model overcomes the difficulties above, while also offering orders of magnitude scale-up advantages over conventional engineered tissues in terms of homogeneity of cell sources and the number of conditions that can be studied in parallel.

Fig. 1 shows an overview of the human organs-on-a-chip. The microfluidic culture device synthesizes minimal functional organ units that recapitulate tissue- and organ-level functions in PDMS. The entire movements are then recorded by Data Acquisition Model (DAM) through the lens. In order to achieve the high-resolution, real-time information, the current DAM deploys a high-resolution microscopy and a high-speed camera, which are expensive and bulky. A low-cost, low-complexity and high-performance DAM solution is urgently demanded to enable POC application of OC.

Compressed Sensing (CS) [4] has achieved significant development in terms of compression and reconstruction in recent years. It is an efficient Analog-to-Information (A2I) framework that simultaneously combines sampling and compression into a single process. Inspired by the work of Duarte *et al.* [5], where a simpler, smaller, and cheaper single pixel camera architecture was presented based on CS, we explore the possibility of applying CS on organ-on-a-chip data acquisition.

Traditional CS approaches usually focus on single data domain, either in spatial (image [6]) or in temporal (bio channel signal [7]). Some CS strategies have been proposed for high-throughput video streams. Reddy *et al.* [8] applied a random mask on each frame and reduced the temporal frames by integrating several encoded frames together before spatial downsampling. Since it only aggregates certain number of frames along the temporal domain, the solution is essentially the one-dimensional CS scheme. Sankaranarayanan *et al.* [9] located similar frames in the digital video via motion estimation to achieve temporal downsampling, which means the architecture needs to digitize each frame first. To the best of our knowledge, there is no similar unified CS architecture for Tempo-Spatial stream that can complete the sensing and compression simultaneously in the analog front-end.

In this paper, we propose a novel unified analog-to-information architecture, namely, TS-CS, which is able to compress the two-dimensional OC information in analog before the digital quantization. TS-CS is a better DAM approach in terms of complexity and cost. It provides better compression-performance tradeoff by efficiently compressing and sensing the OC data in both temporal and spatial domains. We comprehensively evaluate the system performance by employing four different bases for CS. With comparison to the traditional way, we show that TS-CS always obtains better recovery result. In summary, with TS-CS technology, the traditional expensive and bulky OC DAM can be replaced by the low-cost and low-complexity devices.

Our main contributions can be categorized into three aspects:

- 1) TS-CS is a novel direct analog-to-information acquisition framework for tempo-spatial dynamic stream data which consolidates the sensing and compression process together.
- 2) TS-CS is a scalable architecture in both temporal and spatial domains. The user can specify the compression ratio (CR) to achieve the specific performance demand.
- 3) Our experiment shows that TS-CS achieves better performance in most conditions than the traditional CS (individually applying CS on each frame) in terms of reconstruction error and throughput.

The rest of the paper is organized as follows: In Section II, we introduce the background of OC, CS, and high-throughput challenges in OC. In Section III, the detailed architecture of TS-CS is elaborated. In Section IV, we first evaluate the performance of TS-CS with different combinations of CR in the temporal and spatial domain. Then we compare it to the traditional CS in the aspect of reconstruction error and throughput. In Section V, the related work of CS on bio-signals and

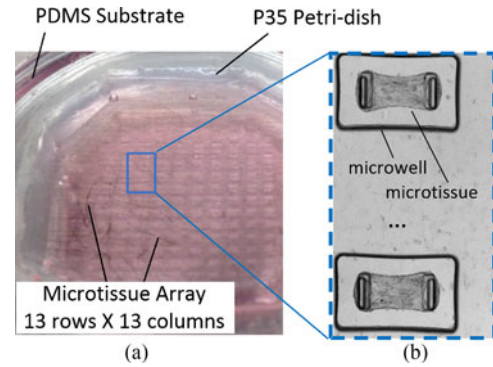


Fig. 2. The organ-on-chip device demonstration. (a) A petri dish with 35 mm diameter contains an array of engineered microtissues (13 rows  $\times$  13 columns) fabricated in a polydimethylsiloxane (PDMS) substrate. (b) The zoom-in of the microtissues. The microtissue lays inside the microwell, which has the size of  $400 \mu\text{m} \times 800 \mu\text{m}$ .

tempo-spatio data processing is introduced. Last, we draw the conclusion in Section VI.

## II. BACKGROUND

### A. Organ-on-a-Chip

For almost a century, two dimensional (2D) cell culture models such as human or animal cells cultured in petridishes have been the main workhorse for the biological research community [10], [11]. While these model systems are easy to setup and operate and contribute to essentially every aspects of biological research, they do not support tissue level modeling including the cellular interaction with the extracellular matrix [12]. These interactions are important to the maintenance of the tissue health and the alteration in these interactions has been found to induce disease formation. The limitation of the 2D model has led to the development of 3D models for biological research, which often consist of cells encapsulated in hydrogels [13]. These models retain important aspects of native tissue, but they require a lot of resources and suffer from limitations in oxygen and nutrient diffusion and very low experimental throughput.

Newly emerged OC models offer the possibility to overcome the above limitations [14], [15]. They are experimental devices created using microelectromechanical systems (MEMS) method, for culturing live cells in micrometer-sized chambers. These devices allow physiologically-relevant modeling of the normal or diseased functions of native tissues in ways not possible by 2D model. Also, due to the miniature size and often array format of the device, OC devices consume much less experimental material and offer much better experimental throughput and nutrient diffusion than the conventional 3D model [16]. OC devices have been developed to model human tissues in brain, lung, kidney, heart and intestine [17]. Fig. 2 give a demonstration of the OC device, where the left subfigure shows that a P35 petri-dish (i.e., a petri dish with 35 mm diameter) contains an array of engineered fibroblast microtissues fabricated in a polydimethylsiloxane (PDMS) substrate and the right subfigure shows that a portion of the microtissue array. Currently, OCs are

mainly used for disease modeling, drug screening and disease diagnosis [14], [18].

### B. High-Throughput Challenge in OC Monitoring

A major advantage of the OC model over conventional 2D and 3D models is the high experimental throughput [19]. Thanks to the adoption of the MEMS fabrication method, OC device often features large array format. It is quite common to create hundreds of samples on one single chip the size of half of a credit card. The image acquisition and multi-parameter data processing for such a large array of samples is very demanding. Furthermore, the integration of a chip with microfluidic channels or mechanical stretching systems can allow dynamic flow or motion to the OC device, to better mimic the blood flow and tissue motion conditions. In the studies of circulating cells such as platelets and red blood cells, hundreds or even thousands of cells can pass through a designated cross-section of a microfluidic channel at the same time. Capturing the signals of these cells and processing these data in a timely manner is also very challenging [20]. Therefore, the development of computational algorithms that can handle large data set with high spatial and temporal resolution is needed to fully utilize the unique features of the OC models.

### C. Compressed Sensing Basics

Compressed sensing is an emerging low-rate sampling scheme for the signals that are known to be sparse or compressible in certain cases. CS has been successfully applied in image processing, pattern recognition, and wireless communications.

We assume  $x$  is an  $N$ -dimension vector and sampled using  $M$ -measurement vector  $y$ :

$$y = \Phi x, \quad (1)$$

where  $\Phi \in R^{M \times N}$  is the sensing array, which models the linear encoding, and  $M$  is defined as the sampling rate in  $N$ -dimension CS. The elements in  $\Phi$  are either Gaussian random variables or Bernoulli random variables. Because  $M \ll N$ , the formulation in (1) is undetermined, and signal  $x$  cannot be uniquely retrieved from sensing array  $\Phi$  and measurements  $y$ . However, under a certain sparsity-inducing basis  $\Psi \in R^{N \times N}$ , the signal  $x$  can be represented by a set of sparse coefficients  $u \in R^N$ :

$$x = \Psi u, \quad (2)$$

that is, the coefficient  $u$ , under the transformation  $\Psi$ , only has few non-zero elements. Therefore, based on (1) and (2), the sparse vector,  $u$ , can be represented as follows:

$$y = \Phi \Psi u = \Theta_{M \times N} u, \quad (3)$$

where  $\Theta_{M \times N} = \Phi \Psi$  is an  $M \times N$  array, called measuring matrix. Due to the prior knowledge that the unknown vector,  $u$ , is sparse, it is possible to estimate the value,  $u$ , using the  $\ell_0$  minimization formulation as follows:

$$u = \min \|u\|_0, \quad s.t. \quad \|y - \Theta u\| < \epsilon, \quad (4)$$

where  $\epsilon$  is the reconstruction error tolerance. The formulation in (4) is a determined system with unique solutions. However,  $\ell_0$

is an NP-hard (non-deterministic polynomial-time hard) problem [21], and one of the methods to solve (4) is to relax  $\ell_0$  minimization formulation to  $\ell_1$  minimization formulation:

$$u = \min \|u\|_1, \quad s.t. \quad \|y - \Theta u\| < \epsilon. \quad (5)$$

Under the condition of Restricted Isometry Property (RIP) [22],  $\ell_1$  has been theoretically proven to be equivalent to minimizing  $\ell_0$ . Moreover,  $\ell_1$  minimization is convex and can be solved within polynomial time. In this work, we will use the  $\ell_1$ -based approach Compressed Sensing. After estimating the sparse coefficient  $u$  with the formulation in (5), the original input signal  $x$  can be recovered as  $\hat{x}$  as:

$$\hat{x} = \Psi u. \quad (6)$$

## III. TEMPO-SPATIAL COMPRESSED SENSING (TS-CS) ARCHITECTURE

### A. Architecture Overview

While the existing CS approaches for high-throughput stream mostly focus in a single domain, we propose TS-CS, a unified CS architecture which combines temporal compression and spatial compression together before quantization. We term the video stream in the form of  $f \times r \times c$ , while  $f$  is the number of the frames and  $r \times c$  is the size of each frame. Fig. 3 shows the overview of the whole dataflow. The original high-throughput OC stream  $S$  is in the size of  $L \times A \times B$ . TS-CS compresses the stream in two domains and outputs the compressed data in the size of  $L' \times A' \times B'$ . After digital quantization, the data is transmitted for reconstruction or compression analysis. As depicted in Fig. 3, TS-CS mainly consists of two phases: *temporal compression phase* and *spatial compression phase*, where the data in the corresponding domain is compressed.

### B. Acquisition Architectures

**1) Temporal Compression Phase:** The goal of this phase is to compress  $S$  from  $L$  into  $\widehat{L}$  frames along the temporal domain ( $\widehat{L} < L$ ). Since the neighboring frames contain the continuous information of the organ movement, we can assume that each pixel array  $P_{ab} = \{p_{ab}^1, \dots, p_{ab}^L\}$  along the temporal domain can be sparsely represented under a certain basis ( $1 \leq a \leq A, 1 \leq b \leq B$ ).

Following the above assumption, we employ a  $\widehat{L} \times L$  sensing matrix,  $M$ , to reduce the dimension of each  $P_{ab}$  in the temporal domain. To achieve that, we duplicate  $S$  into  $\widehat{L}$  channels (see Fig. 4), while  $\{TCP^i | 1 \leq i \leq \widehat{L}\}$  denotes the output frame of the  $i$ th channel. In each channel  $i$ , the corresponding  $i$ th row in  $M$  is applied to modulate each  $P_{ab}$ . Let  $m_{ij}$  be the entry at the  $i$ th row and  $j$ th column in  $M$ . By integrating  $L$  modulated frames, we calculate each pixel in the output matrix as:

$$TCP_{ab}^i = \sum_{j=1}^L p_{ab}^j \times m_{ij}, \quad \forall 1 \leq i \leq \widehat{L}, 1 \leq a \leq A, 1 \leq b \leq B. \quad (7)$$

In this way, we apply CS along the temporal domain and obtain  $\widehat{L}$  frames instead of the original  $L$  ones after Temporal Compression Phase. Note that although each  $TCP^i$  still remains

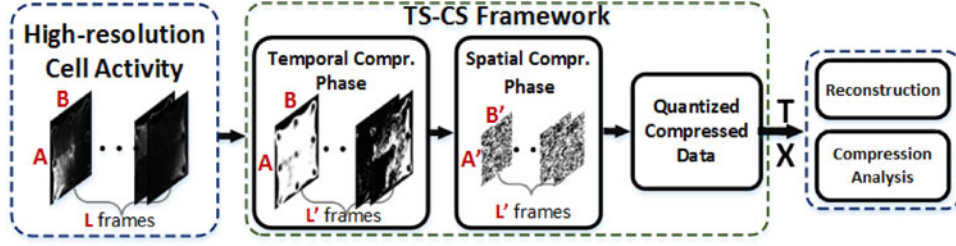


Fig. 3. The overview of TS-CS architecture, which mainly comprises Temporal Compression Phase as well as Spatial Compression Phase. It takes the high-resolution cell activity recording stream as the input and generates the quantized compressed data to improve the throughput. The reconstruction and compression analysis are performed later when we need to recover the original cell activity stream from the compressed data. Note that all the compressed sensing process is conducted in analog domain before the digital quantization module.

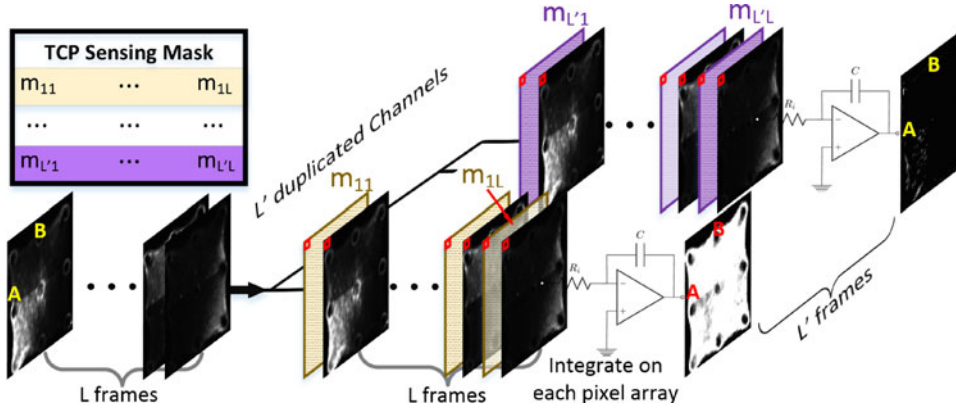


Fig. 4. The structure of Temporal Compression Phase. This phase operates the compression on each image pixel sequence in the temporal domain. By employing the corresponding sensing masks, this phase integrates the sequential information of each pixel sequence into one new pixel.

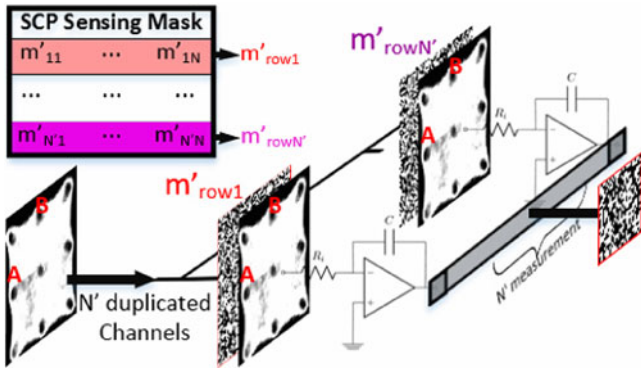


Fig. 5. The structure of Spatial Compression Phase. This phase operates the compression on the image of each channel in the spatial domain. By employing the corresponding sensing masks, this phase integrates all the pixels in each image into one new pixel.

the size of  $A \times B$ , the information contained is actually the fusion of the original  $L$  frames.

2) **Spatial Compression Phase:** In this phase, we conduct compression in the spatial domain to compress the size of each  $TCP^i$  from  $N = A \times B$  to  $N' = A' \times B'$ . Specifically, we generate an  $N' \times N$  sensing matrix,  $M'$ , for the spatial dimension reduction. For each  $TCP^i$  (see Fig. 5), we duplicate the frame into  $N'$  channels. In each channel  $i$ , we set the corresponding  $i$ th row in  $M'$  to modulate the whole frame. For the ease of representation, let  $TCP^i$  be the vectorized form ( $N \times 1$  array) of  $TCP^i$ ,  $m'_{ij}$  be the entry at the  $i$ th row and  $j$ th column in

$M'$  and  $SCP^i$  be the modulation result of  $TCP^i$  after Spatial Compression Phase. The final measurement in each channel  $i$  is the integration of all the modulated pixel values, which can be formulated as:

$$SCP^i_t = \sum_{j=1}^N TCP^i_j \times m'_{ij}, \forall 1 \leq t \leq N', 1 \leq i \leq \hat{L}. \quad (8)$$

Eventually, after converting the result  $SCP^i$  from  $N' \times 1$  to  $A' \times B'$ , we successfully compress the data from  $L \times A \times B$  data into  $L' \times A' \times B'$  and the compression ratio (CR) is defined as  $(L' \times A' \times B') / (L \times A \times B) \times 100\%$ .

It is worth to mention that the duplicate-channel scheme is for the purpose of demonstration. In practice, a control unit can be applied to adjust the modulation mask via Digital Micromirror Device array (DMD) according to the sensing matrix at a rate higher than the acquisition frame rate of the camera. Both low frame-rate video camera and high frame-rate modulator are inexpensive, which therefore results in a significant cost reduction.

### C. Reconstruction

1) **Basis Design:** We applied several well-known basis for our TS-CS architecture and evaluated their performance, including the discrete cosine transform (DCT), the discrete Fourier transform (DFT), the discrete wavelet transform (DWT), and the discrete Walsh-Hadamard transform (WHT).

a) *Discrete Cosine Transform (DCT)*: The DCT, which is based on cosine function, is used to convert an arbitrary signal into elementary frequencies [23]. Specifically, an arbitrary signal  $x$  can be represented as a sum of cosine functions oscillating at different frequencies.

b) *Discrete Fourier Transform (DFT)*: The DFT is most widely used in signal processing, which is the transformation of the discrete signal taking in the time domain into its discrete frequency domain representation, specifically, a set of coefficients of a finite combination of complex sinusoids [24].

c) *Discrete Wavelet Transform (DWT)*: The DWT describes a multi-resolution decomposition process in terms of expansion of a signal onto a set of wavelet basis functions. Mathematically, it can be described as a set of inner products between a finite-length sequence and a discretized wavelet basis, where each inner product results in a wavelet transform coefficient [25].

d) *Discrete Walsh-Hadamard Transform (DWHT)*: The DWHT is an orthogonal transform whose basis functions consist of a set of rectangular discontinuous waveforms that can take the values  $-1, 0$  and  $1$ . The 1-D DWHT of a discrete-time signal  $x$  is defined in [26].

2) *Reconstruction Algorithms*: After receiving the compressed data at the receiver end, we apply the reconstruction algorithm to obtain the original OC stream in the size of  $L \times A \times B$ . Upon the tempo-spatial compressed data, the reconstruction process is in the reverse order of the compression, which means the reconstruction is conducted first in the spatial domain and then in the temporal domain by solving two consecutive  $\ell_1$ -norm minimization problems. Specifically, the reconstruction process in the tempo-spatial CS framework is described as follows:

---

**Algorithm 1: Reconstruction Process.**


---

**Require:**  $y, x, \Phi, \Psi$

**Ensure:**  $y = \Phi \Psi u = \Theta_{M \times N} u$

**Spatial-Phase Reconstruction:**

Given  $y_S, \Phi_S, \Psi_S$  in the spatial compression process

**if**  $x_S$  is sparse under the basis of  $\Psi_S$  **then**

$$u_S = \min \|u_S\|_1, \quad s.t. \quad \|y_S - \Theta_S u_S\| < \epsilon.$$

where

$$\epsilon \leftarrow \text{the signal noise,}$$

$$\Theta_S \leftarrow \Phi_S \Psi_S,$$

$$x_S \leftarrow \Psi_S u_S.$$

**end if**

**Temporal-Phase Reconstruction:**

Given  $y_T, \Phi_T, \Psi_T$  in the spatial compression process

**if**  $x_T$  is sparse under the basis of  $\Psi_T$  **then**

$$u_T = \min \|u_T\|_1, \quad s.t. \quad \|y_T - \Theta_T u_T\| < \epsilon.$$

where

$$\epsilon \leftarrow \text{the signal noise,}$$

$$\Theta_T \leftarrow \Phi_T \Psi_T,$$

$$y_T \leftarrow x_S.$$

**end if**

**Output:**  $x_T \leftarrow \Psi_S u_T$

---

## IV. EVALUATION

### A. Organ-on-a-Chip (OC) Implementation

We employed the fibroblast microtissue to implement the organ-on-a-chip. Specifically, NIH-3T3 fibroblast cells [27] were used to form the fibroblast microtissue. 3T3 cells were cultured in DMEM medium [28] supplemented with 10% fetal bovine serum [29] and 100 (U/ml) Penicillin Streptomycin [30].

Referring to [31]–[33], we employed the multilayer UV-lithography technique to fabricate the SU-8 master of the micro array device on a silicon wafer. Briefly, multilayers of thick SU-8 photoresist were casted on the silicon wafer and exposed to the UV light through the micro array design to construct the leg section of the pillars. Next, the same process was repeated for the head section and by using an alignment machine, the head section was placed on top of the pillars leg. Afterwards, micropillar array pattern was transferred to the polydimethylsiloxane (PDMS) device [34] through soft lithography and replica molding.

After preparing the microdevice, we then proceeded to form microtissues. The 3T3 fibroblasts were collected and seeded into the microtissue array device. The micropillar devices were sterilized in 70% ethanol for 15 minutes before cell seeding and then treated with 0.2% Pluronic, which is a surfactant to reduce the surface adhesiveness of the PDMS and help the cells to uniformly detach and compact the gel in order to create an intended structures. Afterward, unpolymerized rat tail collagen type I [35] was prepared by neutralizing with 1M *NaOH*, and mixed with 3T3 cells and then seeded into the device at a constant cell number of 450,000 cells per device. Consequently, the seeded cell and collagen mixture were polymerized in an incubator at 37°C and under 5% *CO*<sub>2</sub>. Later, the culture media was added to the device. The tissues were formed as cells compacted the collagen gel within 24 hours. Cell culture media was changed every 72 hours.

For immunofluorescence staining, first microtissues were fixed with 4% paraformaldehyde in PBS (phosphate buffer saline) for 10 minutes and permeabilized with Triton X-100 [36]. Next, they were blocked with bovine serum albumin (BSA 3%) for one hour at room temperature and incubated with primary collagen type I antibody [37] diluted in BSA 3% (1:400) overnight at 4°C. Next, the primary collagen type I antibody was counterstained with secondary anti-IgG antibodies [38]. In order to stain the nuclei, we used Hoechst stain [39] at 1:1000 dilution ratio in PBS.

### B. Dataset and Metrics

To record the tissue behavior, we employed a Zeiss LSM-510 Meta confocal microscope with a Plan-Apochromat 20X air objective in 1.5  $\mu\text{m}$  optical slices for all channels. For each microtissue imaged, a 450  $\mu\text{m}$   $\times$  209  $\mu\text{m}$  area is scanned through an approximately 80  $\mu\text{m}$  thickness. The stack of images obtained in confocal microscopy is used as original OC data. Eventually, we achieved the OC stream with the size of 34  $\times$  64  $\times$  40 to quantitatively evaluate the advantage of TS-CS.

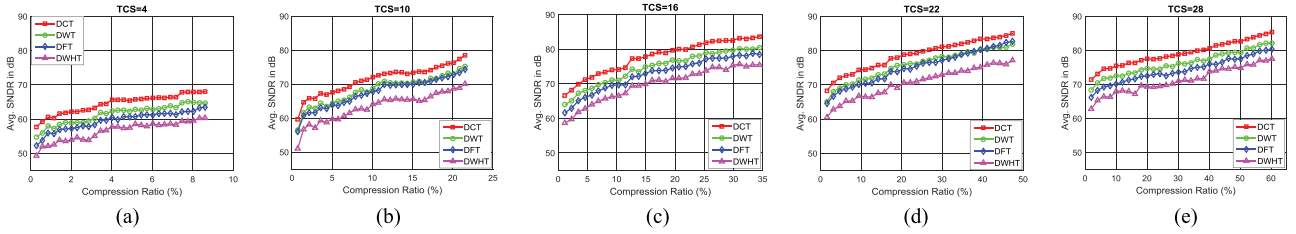


Fig. 6. The comparison of reconstruction results of TS-CS in terms of average SNDR versus compression ratio. We group the performance results based on the adopted bases and show the results with different TCS configuration in each subfigure. (a) TCS = 4. (b) TCS = 10. (c) TCS = 16. (d) TCS = 22. (e) TCS = 28.

We implement TS-CS architecture as well as the traditional CS approach (denoted as Tra-CS), which individually applied CS on each frame. We generate the random matrix (Bernoulli for TCS and Gaussian for SCS [40]) to be the sensing matrix  $\Phi$  and employ different matrix as the basis  $\Psi$ , which is specified in Section II-C. Let TCS and SCS be the measurement settings in Temporal Compression Phase and Spatial Compression Phase. In TS-CS, the combination of 10 TCS ([1, 4, 7, 10, 13, 16, 19, 22, 25, 28]) and 30 SCS (from 100 ~ 3000 with the step of 100) are simulated. The same 30 SCS are simulated with Tra-CS. The recovery error is measured by Signal to Noise and Distortion Ratio (SNDR):

$$SNDR = 20 \log \frac{\|x_t\|_2}{\|x_t - \hat{x}_t\|_2}, \quad (9)$$

where  $x_t$  is the original vectorized frame and  $\hat{x}_t$  is the reconstructed one. Specifically, we calculate the average SNDR of 34 frames.

C. Result Analysis

1) Comparison of Reconstruction Results of TS-CS: We investigated the reconstruction results of TS-CS with different measurement settings of  $TCS = 4, 10, 16, 22, 28$ . We only show partially selected results here for the purpose of visualization. As shown in Fig. 6, the average SNDR gradually grows when CR increases (choose larger SCS) under a given TCS. The performance experiences fluctuation when TCS is relatively small (eg., TCS = 4 or 10). This is understandable because smaller TCS means fewer measurements of each pixel array in the temporal domain. However, when TCS keeps increasing, the performance improves in a monotonous way with some minor artifacts, which is introduced by the performance variation of random sensing matrix and reconstruction algorithm. For any given TCS, the basis of DCT has the highest average SNDR, then DWT and DFT, while DWHT is the lowest. In addition, we also grouped the results in terms of TCS, as shown in Fig. 7. We observed that comparing the performance across different TCS settings using a specific basis, larger TCS has the higher average SNDR, especially, such phenomena are prominent when TCS is less than 16.

2) Reconstruction Result of Heatmap: We explored the reconstruction result of TS-CS when applying different TCS and SCS. Fig. 8 depicts the heatmap of the reconstruction result under different TCS/SCS. The color in each grid is correlated to SNDR under the corresponding setting. Generally, the

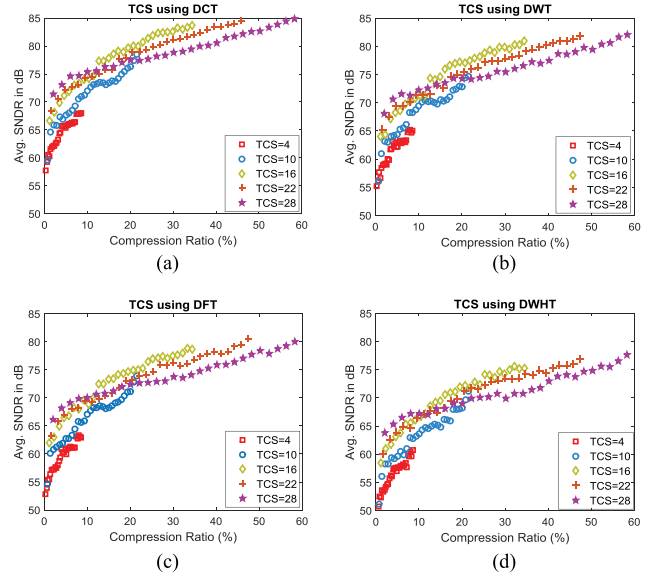


Fig. 7. The reconstruction result of TS-CS with different TCS and SCS, where the results are grouped in terms of TCS. Each subfigure represents different basis adopted for CS. (a) DCT. (b) DWT. (c) DFT. (d) DWHT.

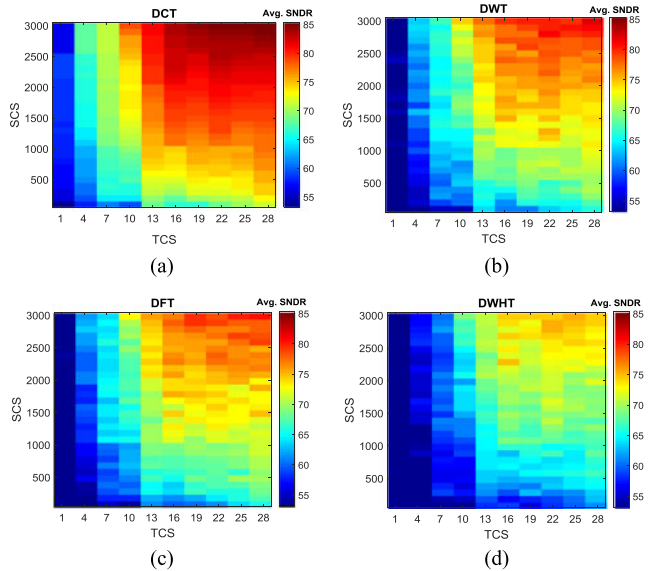


Fig. 8. The heatmap of the reconstruction result of TS-CS in term of different bases. The larger the SNDR value, the better the reconstruction performance. In general, the reconstruction performance is enhanced with the increase of TCS and SCS. Among the four bases, DCT basis achieves the best result. (a) DCT. (b) DWT. (c) DFT. (d) DWHT.

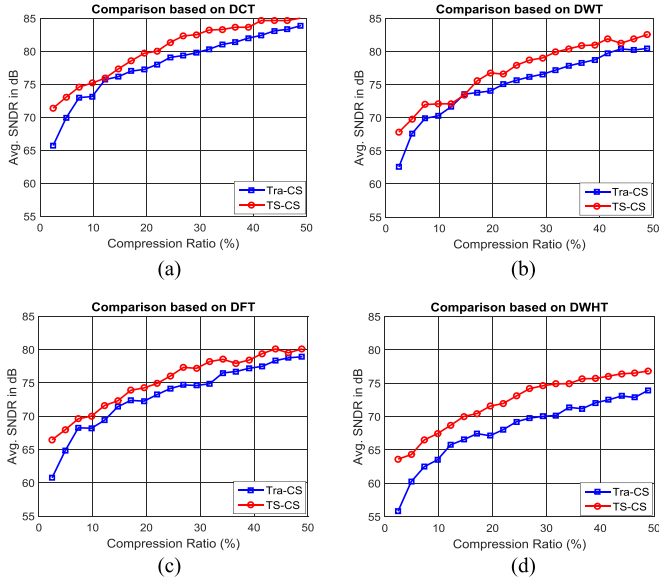


Fig. 9. The comparison between TS-CS and Tra-CS in terms of average SNDR versus compression ratio. (a) DCT. (b) DWT. (c) DFT. (d) DWHT.

reconstruction performance improves with the increase of TCS and SCS. The top right corner with larger TCS and SCS achieves better performance compared with the rest. We also noticed the heatmap of DCT is filled with more dark red color and less deep blue color comparing with other bases, which indicates the DCT has higher average SNDR. Likewise, DWT and DFT have the similar performance, while DWHT has the lowest average SNDR. Such results are coherent with those results presented in Fig. 6.

3) *Comparison Between TS-CS and Tra-CS*: To compare TS-CS with the traditional one in terms of reconstruction result, we first simulate Tra-CS on each frame with 20 different SCS, resulting in 20 reference CR and SNDR. We set each CR as the upper bound, and search for all the possible TCS/SCS pairs in TS-CS that have a smaller CR. Within all the pairs found, we choose the pair with the best performance as the optimal pair and compare it to the performance of Tra-CS. As shown in Fig. 9, the reconstruction result of Tra-CS is plotted in blue square, and the corresponding TS-CS optimal pair is plotted in the red circle.

As we can see the results in Fig. 9, TS-CS achieves better recovery result than Tra-CS along all SCS (100 ~ 2000). Specifically, we define the performance improvement as:

$$REC_{enhance} = \frac{SNDR(TS - CS) - SNDR(Tra - CS)}{SNDR(Tra - CS)}. \quad (10)$$

As a result, the performance improvement that TS-CS outperforms Tra-CS is shown in Table I in terms of SNDR. As can be seen from the table that through DWHT has lowest average SNDR it shows the maximum performance improvement of 16.3%. All other bases including DCT, DWT, and DFT are with close improvement values as 8.6%, 7.9%, 8.7%.

With the above observation, we can prudentially draw a conclusion that given a CR upper bound, there is always a pair of

TABLE I  
PERFORMANCE IMPROVEMENT OF DIFFERENT BASES

	DCT	DWT	DFT	DWHT
$REC_{enhance}$ (%)	8.6	7.9	8.7	16.3
$TP_{enhance}$ (%)	25.0	24.7	23.9	27.5

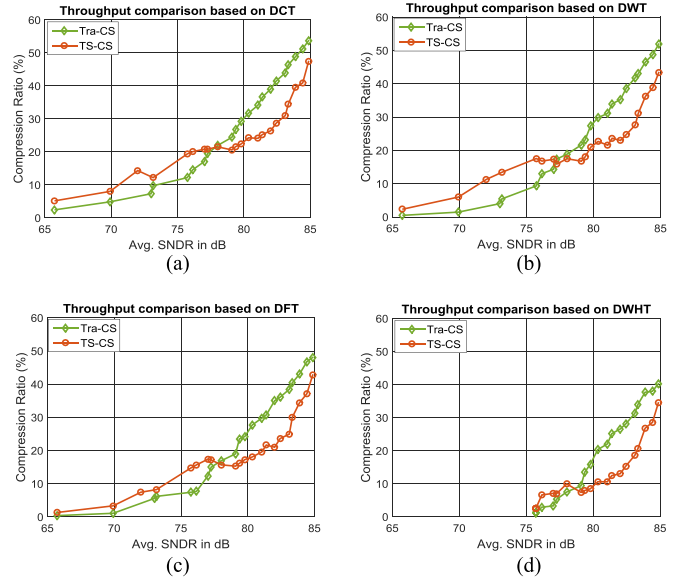


Fig. 10. The comparison between TS-CS and Tra-CS in terms of compression ratio versus average SNDR. (a) DCT. (b) DWT. (c) DFT. (d) DWHT.

TCS/SCS in TS-CS that can achieve better performance than Tra-CS.

4) *Reconstruction Result of Throughput*: We also compare TS-CS with Tra-CS in terms of throughput. With 20 SNDR in Tra-CS obtained above, we set each as the performance lower bound, and search for all the possible TCS/SCS pairs in TS-CS that obtain higher average SNDR. Within all the pairs found, we choose the pair with the smallest CR as the optimal pair and compare with the results in Tra-CS.

As shown in Fig. 10, the results can be categorized into two cases. When the performance bound is small (average SNDR < around 78), the closest performance is achieved with small CR ( $\leq 20\%$ ), which can lead to larger performance fluctuation and additional recovery variation because there are two reconstruction steps in TS-CS. These variations cause the result that the CR of the optimal pair in TS-CS is larger than the reference one in Tra-CS. However, when the performance bound is larger than a certain threshold (average SNDR > round 78), the optimal pair in TS-CS consistently obtains a smaller CR than Tra-CS (smaller CR means larger throughput). The higher throughput means more data acquisition and less energy consumption in transmission. Particularly, we define the throughput enhancement as:

$$TP_{enhance} = \frac{CR(Tra - CS) - CR(TS - CS)}{CR(Tra - CS)}. \quad (11)$$

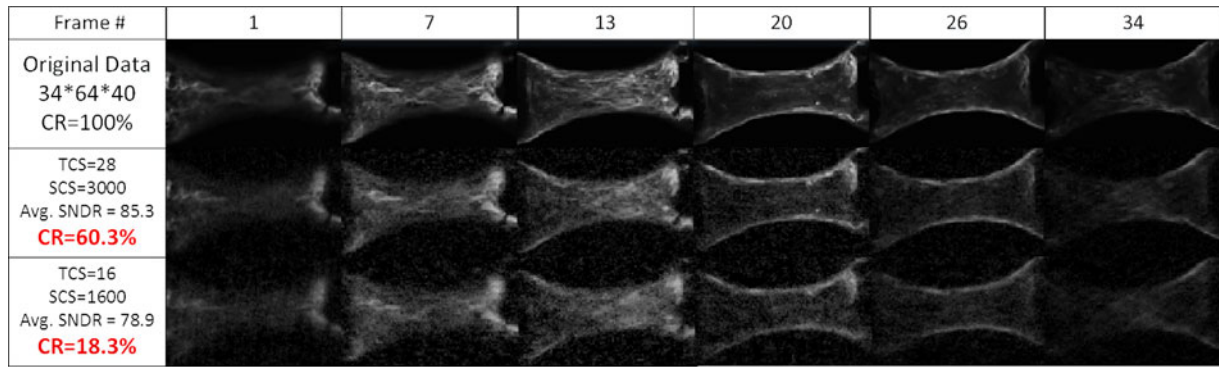


**Fig. 11.** A demonstration of the real OC data and the reconstructed ones by TS-CS. The fibroblast microtissue is adopted in this real case study, which is comprised of 34 frames in total and each frame has the pixel dimension of  $64 \times 40$ . The first row is the original data, second row is the result with  $CR = 60.3\%$ , and the third row with  $CR = 18.3\%$ .

The average throughput improvement that TS-CS achieves over Tra-CS is also summarized in Table I, where DWHT has the largest throughput enhancement of 27.5% and others also have comparable enhancement as 25.0%, 24.7%, and 23.9% for DCT, DWT, and DFT, respectively.

#### D. Case Study

In this section, we give direct reconstruction illustration of TS-CS over the aforementioned microtissue steam. We compare each reconstructed frame with the original one to verify whether our proposed CS framework causes any defect in tissue activity monitoring. In Fig. 11, we select 6 frames out of 34 considering the demonstration space. The original data without compression is shown in the first row, which records the entire organ movement. We can see the shape of the tissue varies from obscure to clear, then to obscure again. The second row shows the reconstruction results adopting TS-CS with the configuration of  $TCS = 28$  and  $SCS = 3000$ , equivalent to  $CR \approx 60.3\%$ . While achieving average  $SNDR = 85.3$ , the reconstructed frames of TS-CS can precisely reserve the details of the original ones. If we keep reducing  $CR$  down to average  $SNDR = 78.9$  and  $CR \approx 18.3\%$  with the setting of  $TCS = 16$  and  $SCS = 1600$ , TS-CS can still achieve reliable performance, as the whole movement pattern can be clearly observed. Therefore, TS-CS is a promising high-throughput model for OC data acquisition.

### V. RELATED WORK

#### A. Compressed Sensing for One Dimensional Signal

CS has been widely applied in bio-signal processing due to their sparsity nature in one dimension, such as electroencephalography (EEG), Electrocardiograph (ECG), Electromyography (EMG), and human activities signals. Fauvel *et al.* [41] presented the CS architecture for EEG telemonitoring with a constant bit resolution of quantization. Shukla and Majumdar [42] exploited the inter-channel correlation of EEG signals and used CS framework for recovering row-sparse signal ensembles in multichannel EEG signals. The work is later extended by Majumdar and Ward [43] by considering the ensembles' approximate rank deficiency in addition to exploit the sparsity of the multi-channel ensemble in a learned basis. Liu *et al.*

[44] adopted CS as a low-power compression approach and proposed a fast block sparse Bayesian learning algorithm to reconstruct ECG and EEG signals. Other works [45]–[47] also applied CS for ECG signals considering the time-domain sparsity nature of the signal and quantization noise. Wang *et al.* [48] presented a novel configurable quantized CS architecture and a rapid RapQCS algorithm for the energy efficient sampling and wireless transmission of bio-signals, in which the sampling rate and quantization are jointly explored for better energy efficiency. By taking into account of the time-varying sparsity nature of bio-signals, the same team later proposed a dynamic knob design [49], which is a template-based structure that comprises a supervised learning module and a look-up table module, to effectively and adaptively reconfigure the CS architecture by recognizing the bio-signals. Wang *et al.* [50], [51] and Song *et al.* [52] designed a new selective CS architecture for wireless implantable neural decoding by adopting a two-stage classification procedure. Xu *et al.* [53] presented a CS-based approach to co-recognize human activity and sensor location in a single framework without knowing the sensor location information as a prior. Zhao *et al.* [54] proposed an adaptive CS solution based on the block sparsity of the image. Fallahzadeh *et al.* [55] used a coarse-grained activity recognition module to adaptively tune the compressed sensing module to minimize sensing/transmission costs.

#### B. Compressed Sensing for Video Data

Compressed Sensing is also adopted in the research of temporal data processing. Works [56]–[58] proposed adaptive approaches to conduct compressed sensing on each frame. Do *et al.* [59] proposed a distributed compressed video sensing which recovers video frames jointly at the decoder by exploiting an inter-frame sparsity model and by performing sparse recovery with side information. Pudlewski *et al.* [60] presented a design of a networked system for joint compression, rate control, and error correction of video over resource-constrained embedded devices based on the theory of CS for the purpose of maximizing the received video quality. Hosseini *et al.* [61] proposed a model to the total variation regularization problem to regulate the spatial and temporal redundancy in compressed video sensing for jointly recovering frames from under-sampled measurements.

Guo *et al.* [62] proposed a method based on CS to obtain a trained dictionary directly by using the measurements of the video data, and then keep the sparse components and generate a saliency map. Chen and Chau [63] developed a CS framework for the sampling and reconstruction of a high-resolution light field data based on a coded aperture camera. Chen *et al.* [64] proposed a tempo-spatial sparse representation based recovery by considering the spatial and temporal correlations of the video sequence. Sung *et al.* [65] presented a novel iterative thresholding method, called Location Constrained Approximate Message Passing, to reduce computational complexity and improve reconstruction accuracy in CS for the magnetic resonance imaging processing.

## VI. CONCLUSION

In this paper, we presented TS-CS, a novel A2I architecture for high-throughput OC video which truly combines sensing with compression along the temporal and spatial domains. We employed a real OC data and evaluated the performance of TS-CS. The comparison between TS-CS with Tra-CS showed that TS-CS achieved better reconstruction when given a throughput upper bound and continuously obtained larger throughput after the reconstruction lower bound exceeded a threshold. Specifically, we explored different basis and proved that DWHT performs better for the particularly employed fibroblast tissue. For other tissues, the optimal basis can be decided by following the same methodology. The case study illustrated the reconstruction performance of TS-CS under low CR. Our future work involves adapting programmable A2I converter architecture [66], [67], memristor-based hardware acceleration architecture [68], [69], and “XPro” cross-end analytic engine architecture [70] for OC data acquisition to enable effective configurability and reduce its energy overhead by integrating efficient multiplexing hardware design.

## REFERENCES

- [1] C. Song, A. Wang, F. Lin, R. Zhao, Z. Jin, and W. Xu, “A tempo-spatial compressed sensing architecture for efficient high-throughput information acquisition in organs-on-a-chip,” in *Proc. 2017 IEEE EMBS Int. Conf. Biomed. Health Inform.*, Feb. 2017, pp. 229–232.
- [2] S. N. Bhatia and D. E. Ingber, “Microfluidic organs-on-chips,” *Nature Biotechnol.*, vol. 32, pp. 760–772, 2014.
- [3] D. Huh, Y.-S. Torisawa, G. A. Hamilton, H. J. Kim, and D. E. Ingber, “Microengineered physiological biomimicry: Organs-on-chips,” *Lab Chip*, vol. 12, no. 12, pp. 2156–2164, 2012.
- [4] D. L. Donoho, “Compressed sensing,” *IEEE Trans. Inf. Theory*, vol. 52, no. 4, pp. 1289–1306, Apr. 2006.
- [5] M. F. Duarte *et al.*, “Single-pixel imaging via compressive sampling,” *IEEE Signal Process. Mag.*, vol. 25, no. 2, pp. 83–91, Mar. 2008.
- [6] M. Lustig, D. Donoho, and J. M. Pauly, “Sparse MRI: The application of compressed sensing for rapid MR imaging,” *Magn. Reson. Med.*, vol. 58, no. 6, pp. 1182–1195, 2007.
- [7] T. Xiong *et al.*, “A dictionary learning algorithm for multi-channel neural recordings,” in *Proc. 2014 IEEE Biomed. Circuits Syst. Conf.*, 2014, pp. 9–12.
- [8] D. Reddy, A. Veeraraghavan, and R. Chellappa, “P2C2: Programmable pixel compressive camera for high speed imaging,” in *Proc. 2011 IEEE Conf. Comput. Vision Pattern Recog.*, 2011, pp. 329–336.
- [9] A. C. Sankaranarayanan, C. Studer, and R. G. Baraniuk, “CS-MUVI: Video compressive sensing for spatial-multiplexing cameras,” in *Proc. 2012 IEEE Int. Conf. Comput. Photography*, 2012, pp. 1–10.
- [10] R. H. Schwartz *et al.*, “A cell culture model for t lymphocyte clonal energy,” *Science*, vol. 248, no. 4961, pp. 1349–1356, 1990.
- [11] L. Rubin *et al.*, “A cell culture model of the blood-brain barrier,” *J. Cell Biol.*, vol. 115, no. 6, pp. 1725–1735, 1991.
- [12] F. Bonnier *et al.*, “Cell viability assessment using the alamar blue assay: A comparison of 2d and 3d cell culture models,” *Toxicology Vitro*, vol. 29, no. 1, pp. 124–131, 2015.
- [13] M. W. Tibbitt and K. S. Anseth, “Hydrogels as extracellular matrix mimics for 3d cell culture,” *Biotechnol. Bioeng.*, vol. 103, no. 4, pp. 655–663, 2009.
- [14] J. D. Caplin, N. G. Granados, M. R. James, R. Montazami, and N. Hashemi, “Microfluidic organ-on-a-chip technology for advancement of drug development and toxicology,” *Adv. Healthcare Mater.*, vol. 4, no. 10, pp. 1426–1450, 2015.
- [15] M. Mehling and S. Tay, “Microfluidic cell culture,” *Curr. Opinion Biotechnol.*, vol. 25, pp. 95–102, 2014.
- [16] F. Xu *et al.*, “A microfabricated magnetic actuation device for mechanical conditioning of arrays of 3d microtissues,” *Lab Chip*, vol. 15, no. 11, pp. 2496–2503, 2015.
- [17] D. Huh *et al.*, “Microfabrication of human organs-on-chips,” *Nature Protocols*, vol. 8, no. 11, pp. 2135–2157, 2013.
- [18] A. Skardal, T. Shupe, and A. Atala, “Organoid-on-a-chip and body-on-a-chip systems for drug screening and disease modeling,” *Drug Discovery Today*, vol. 21, no. 9, pp. 1399–1411, 2016.
- [19] G. Du, Q. Fang, and J. M. den Toonder, “Microfluidics for cell-based high throughput screening platforms a review,” *Anal. Chim. Acta*, vol. 903, pp. 36–50, 2016.
- [20] Z. Chen *et al.*, “Lung microtissue array to screen the fibrogenic potential of carbon nanotubes,” *Sci. Rep.*, vol. 6, 2016, Art. no. 31304.
- [21] A. Paz and S. Moran, “Non deterministic polynomial optimization problems and their approximations,” *Theor. Comput. Sci.*, vol. 15, no. 3, pp. 251–277, 1981.
- [22] A. M. Tillmann and M. E. Pfetsch, “The computational complexity of the restricted isometry property, the nullspace property, and related concepts in compressed sensing,” *IEEE Trans. Inf. Theory*, vol. 60, no. 2, pp. 1248–1259, Feb. 2014.
- [23] W.-H. Chen, C. Smith, and S. Fralick, “A fast computational algorithm for the discrete cosine transform,” *IEEE Trans. Commun.*, vol. C-25, no. 9, pp. 1004–1009, Sep. 1977.
- [24] S. Schmale, B. Knoop, J. Hoeffmann, D. Peters-Drolshagen, and S. Paul, “Joint compression of neural action potentials and local field potentials,” in *Proc. 2013 Asilomar Conf. Signals, Syst. Comput.*, 2013, pp. 1823–1827.
- [25] L. M. Bruce, C. H. Koger, and J. Li, “Dimensionality reduction of hyperspectral data using discrete wavelet transform feature extraction,” *IEEE Trans. Geosci. Remote Sens.*, vol. 40, no. 10, pp. 2331–2338, Oct. 2002.
- [26] R. Costantini, J. Bracamonte, G. Ramponi, J.-L. Nagel, M. Ansorge, and F. Pellandini, “A low-complexity video coder based on the discrete Walsh Hadamard transform,” in *Proc. 2000 10th Eur. Signal Process. Conf.*, 2000, pp. 1–4.
- [27] “NIH-3T3 Cell.” [Online]. Available: <https://www.atcc.org/products/all/CRL-1658.aspx>. Accessed on: Sep. 12, 2017.
- [28] “DMEM Medium.” [Online]. Available: <https://www.thermofisher.com/order/catalog/product/11965092>. Accessed on: Sep. 12, 2017.
- [29] “Fetal Bovine Serum.” [Online]. Available: <https://www.thermofisher.com/order/catalog/product/26140079>. Accessed on: Sep. 12, 2017.
- [30] “Penicillin Streptomycin.” [Online]. Available: <https://www.thermofisher.com/order/catalog/product/1514108>. Accessed on: Sep. 12, 2017.
- [31] W. R. Legant, A. Pathak, M. T. Yang, V. S. Deshpande, R. M. McMeeking, and C. S. Chen, “Microfabricated tissue gauges to measure and manipulate forces from 3d microtissues,” *Proc. Nat. Acad. Sci. USA*, vol. 106, no. 25, pp. 10097–10102, 2009.
- [32] R. Zhao, T. Boudou, W.-G. Wang, C. S. Chen, and D. H. Reich, “Decoupling cell and matrix mechanics in engineered microtissues using magnetically actuated microcantilevers,” *Adv. Mater.*, vol. 25, no. 12, pp. 1699–1705, 2013.
- [33] R. Zhao, C. S. Chen, and D. H. Reich, “Force-driven evolution of mesoscale structure in engineered 3d microtissues and the modulation of tissue stiffening,” *Biomaterials*, vol. 35, no. 19, pp. 5056–5064, 2014.
- [34] “Polydimethylsiloxane.” [Online]. Available: <https://www.ellsworth.com/products/by-market/consumer-products/encapsulants/silicone/dow-corning-sylgard-184-silicone-encapsulant-clear-0.5-kg-kit/>. Accessed on: Sep. 12, 2017.
- [35] “Collagen I, Rat Tail.” [Online]. Available: [https://catalog2.corning.com/LifeSciences/en-US/Shopping/ProductDetails.aspx?productId=354236\(Lifesciences\)](https://catalog2.corning.com/LifeSciences/en-US/Shopping/ProductDetails.aspx?productId=354236(Lifesciences)). Accessed on: Sep. 12, 2017.

- [36] "Triton X-100." [Online]. Available: [http://www.dow.com/assets/attachments/business/pcm/triton/triton\\_x-100/tds/triton\\_x-100.pdf](http://www.dow.com/assets/attachments/business/pcm/triton/triton_x-100/tds/triton_x-100.pdf). Accessed on: Sep. 12, 2017.
- [37] "Collagen Type I Antibody." [Online]. Available: <http://www.abcam.com/collagen-i-antibody-ab34710.html>. Accessed on: Sep. 12, 2017.
- [38] "Anti-IgG Antibodies." [Online]. Available: <https://www.thermofisher.com/antibody/product/Goat-anti-Mouse-IgG-H-L-Cross-Adsorbed-Antibody-Polyclonal>. Accessed on: Sep. 12, 2017.
- [39] "Hoechst Stain." [Online]. Available: <http://biotech.illinois.edu/sites/biotech.illinois.edu/files/uploads/Hoechst.pdf>. Accessed on: Sep. 12, 2017.
- [40] R. Baraniuk, M. Davenport, R. DeVore, and M. Wakin, "A simple proof of the restricted isometry property for random matrices," *Constructive Approx.*, vol. 28, no. 3, pp. 253–263, 2008.
- [41] S. Fauvel and R. K. Ward, "An energy efficient compressed sensing framework for the compression of electroencephalogram signals," *Sensors*, vol. 14, no. 1, pp. 1474–1496, 2014.
- [42] A. Shukla and A. Majumdar, "Row-sparse blind compressed sensing for reconstructing multi-channel EEG signals," *Biomed. Signal Process. Control*, vol. 18, pp. 174–178, 2015.
- [43] A. Majumdar and R. K. Ward, "Energy efficient EEG sensing and transmission for wireless body area networks: A blind compressed sensing approach," *Biomed. Signal Process. Control*, vol. 20, pp. 1–9, 2015.
- [44] B. Liu, Z. Zhang, G. Xu, H. Fan, and Q. Fu, "Energy efficient telemonitoring of physiological signals via compressed sensing: A fast algorithm and power consumption evaluation," *Biomed. Signal Process. Control*, vol. 11, pp. 80–88, 2014.
- [45] E. G. Allstot, A. Y. Chen, A. M. Dixon, D. Gangopadhyay, and D. J. Allstot, "Compressive sampling of ECG bio-signals: Quantization noise and sparsity considerations," in *Proc. Biomed. Circuits Syst. Conf.*, 2010, pp. 41–44.
- [46] E. G. Allstot, A. Y. Chen, A. M. Dixon, D. Gangopadhyay, H. Mitsuda, and D. J. Allstot, "Compressed sensing of ECG bio-signals using one-bit measurement matrices," in *Proc. 9th Int. New Circuits Syst. Conf.*, 2011, pp. 213–216.
- [47] A. Singh and S. Dandapat, "Exploiting multi-scale signal information in joint compressed sensing recovery of multi-channel ECG signals," *Biomed. Signal Process. Control*, vol. 29, pp. 53–66, 2016.
- [48] A. Wang, F. Lin, Z. Jin, and W. Xu, "A configurable energy-efficient compressed sensing architecture with its application on body sensor networks," *IEEE Trans. Ind. Informat.*, vol. 12, no. 1, pp. 15–27, Feb. 2016.
- [49] A. Wang, F. Lin, Z. Jin, and W. Xu, "Ultra-low power dynamic knob in adaptive compressed sensing towards biosignal dynamics," *IEEE Trans. Biomed. Circuits Syst.*, vol. 10, no. 3, pp. 579–592, Jun. 2016.
- [50] A. Wang, C. Song, X. Xu, F. Lin, Z. Jin, and W. Xu, "Selective and compressive sensing for energy-efficient implantable neural decoding," in *Proc. Biomed. Circuits Syst. Conf.*, 2015, pp. 1–4.
- [51] A. Wang, C. Song, Z. Jin, and W. Xu, "Adaptive compressed sensing architecture in wireless brain computer interface," in *Proc. 52nd ACM/IEEE Conf. Design Autom. Conf.*, San Francisco, CA, Jun. 2015, pp. 1–6.
- [52] C. Song, A. Wang, F. Lin, and W. Xu, "Selective CS: Energy-efficient sensing architectures for wireless implantable neural decoding," *IEEE J. Emerging Sel. Topics Circuits Syst.*, vol. 7, no. 12, pp. 218–227, Dec. 2017.
- [53] W. Xu, M. Zhang, A. Sawchuk, and M. Sarrafzadeh, "Co-recognition of human activity and sensor location via compressed sensing in wearable body sensor networks," in *Proc. IEEE Conf. Implantable Wearable Body Sensor Netw.*, London, May 2012, pp. 124–129.
- [54] J. Zhang, Q. Xiang, Y. Yin, C. Chen, and X. Luo, "Adaptive compressed sensing for wireless image sensor networks," *Multimedia Tools Appl.*, vol. 76, no. 3, pp. 4227–4242, 2017.
- [55] R. Fallahzadeh, J. P. Ortiz, and H. Ghasemzadeh, "Adaptive compressed sensing at the fingertip of internet-of-things sensors: An ultra-low power activity recognition," in *Proc. 2017 Design, Autom. Test Eur. Conf. Exhib.*, 2017, pp. 996–1001.
- [56] Z. Liu, A. Y. Elezabi, and H. V. Zhao, "Maximum frame rate video acquisition using adaptive compressed sensing," *IEEE Trans. Circuits Syst. Video Technol.*, vol. 21, no. 11, pp. 1704–1718, Nov. 2011.
- [57] Y. Liu and D. A. Pados, "Compressed-sensed-domain L1-PCA video surveillance," *IEEE Trans. Multimedia*, vol. 18, no. 3, pp. 351–363, Mar. 2016.
- [58] Y. Liu, M. Li, and D. A. Pados, "Motion-aware decoding of compressed-sensed video," *IEEE Trans. Circuits Syst. Video Technol.*, vol. 23, no. 3, pp. 438–444, Mar. 2013.
- [59] T. T. Do, Y. Chen, D. T. Nguyen, N. Nguyen, L. Gan, and T. D. Tran, "Distributed compressed video sensing," in *Proc. 16th IEEE Int. Conf. Image Process.*, 2009, pp. 1393–1396.
- [60] S. Pudlewski, A. Prasanna, and T. Melodia, "Compressed-sensing-enabled video streaming for wireless multimedia sensor networks," *IEEE Trans. Mobile Comput.*, vol. 11, no. 6, pp. 1060–1072, Jun. 2012.
- [61] M. S. Hosseini and K. N. Plataniotis, "High-accuracy total variation with application to compressed video sensing," *IEEE Trans. Image Process.*, vol. 23, no. 9, pp. 3869–3884, Sep. 2014.
- [62] J. Guo, B. Song, and X. Du, "Significance evaluation of video data over media cloud based on compressed sensing," *IEEE Trans. Multimedia*, vol. 18, no. 7, pp. 1297–1304, Jul. 2016.
- [63] J. Chen and L.-P. Chau, "Light field compressed sensing over a disparity-aware dictionary," *IEEE Trans. Circuits Syst. Video Technol.*, vol. 27, no. 4, pp. 855–865, Apr. 2017.
- [64] W. Che, X. Gao, X. Fan, F. Jiang, and D. Zhao, "Spatial-temporal recovery for hierarchical frame based video compressed sensing," in *Proc. 2015 IEEE Int. Conf. Image Process.*, 2015, pp. 1110–1114.
- [65] K. Sung, M. Saranathan, B. L. Daniel, and B. A. Hargreaves, "High spatio-temporal resolution dynamic contrast-enhanced MRI using compressed sensing," in *Proc. 2012 Asia-Pac. Signal Inf. Process. Assoc. Annu. Summit Conf.*, 2012, pp. 1–6.
- [66] A. Wang, Z. Jin, and W. Xu, "A programmable analog-to-information converter for agile biosensing," in *Proc. 2016 Int. Symp. Low Power Electron. Design*, 2016, pp. 206–211.
- [67] A. Wang, C. Song, and W. Xu, "A configurable quantized compressed sensing architecture for low-power tele-monitoring," in *Proc. Int. Green Comput. Conf.*, Dallas, TX, Nov. 2014, pp. 1–10.
- [68] X. Xu *et al.*, "Accelerating dynamic time warping with memristor-based customized fabrics," vol. 20, no. 1, pp. 1–12, Jan. 2018.
- [69] X. Xu, D. Zeng, W. Xu, Y. Shi, and Y. Hu, "An efficient memristor-based distance accelerator for time series data mining on data centers," in *Proc. 54th Annu. Design Autom. Conf.*, 2017, pp. 58:1–58:6.
- [70] A. Wang, L. Chen, and W. Xu, "XPro: A cross-end processing architecture for data analytics in wearables," in *Proc. 44th Annu. Int. Symp. Comput. Archit.*, Toronto, ON, Jun. 2017, pp. 69–80.